JGR Oceans

RESEARCH ARTICLE

10.1029/2021JC017781

Key Points:

- Shoaling nonlinear internal solitary waves were observed over three fortnights using moorings and an optical cable from 2000 m depth to the top of Dongsha Reef in the South China Sea
- Packet formation was common from the 500 to 300 m isobaths but almost all waves broke by the time they reached 100 m depth and subsequently presented a turbulent, transformed wave runup environment
- Possible outcomes are classified according to the wave type, incident wave amplitude, propagation direction, and ambient stratification

Correspondence to:

S. R. Ramp,
sramp@solitonocean.com

Citation:

Ramp, S. R., Yang, Y.-J., Jan, S., Chang, M.-H., Davis, K. A., Sinnett, G., et al. (2022). Solitary waves impinging on an isolated tropical reef: Arrival patterns and wave transformation under shoaling. *Journal of Geophysical Research: Oceans*, *127*, e2021JC017781. https://doi.org/10.1029/2021JC017781

Received 14 JUL 2021
Accepted 18 FEB 2022

Solitary Waves Impinging on an Isolated Tropical Reef: Arrival Patterns and Wave Transformation Under Shoaling

S. R. Ramp[1], Y.-J. Yang[2], S. Jan[2], M.-H. Chang[2], K. A. Davis[3], G. Sinnett[3], F. L. Bahr[4], D. B. Reeder[5], D. S. Ko[6], and G. Pawlak[7]

[1]Soliton Ocean Services, LLC, Falmouth, MA, USA, [2]Institute of Oceanography, National Taiwan University, Taipei, Taiwan, [3]Department of Earth System Science and Civil and Environmental Engineering, University of California Irvine, Irvine, CA, USA, [4]Monterey Bay Aquarium Research Institute, Moss Landing, CA, USA, [5]Naval Postgraduate School, Monterey, CA, USA, [6]Naval Research Laboratory, Stennis Space Center, MS, USA, [7]Department of Mechanical and Aerospace Engineering, University of California San Diego, San Diego, CA, USA

Abstract Large nonlinear internal solitary waves (NLIWs) are known to transit west northwest across the northeastern South China Sea from generation sites around the two-ridge system in the Luzon Strait. The waves are important because their energy flux and dissipation are several orders of magnitude larger than the surrounding ocean. The wave transit has been well studied up to about the 100 m isobath but observations in shallower water have been scarce. Using oceanographic moorings and an innovative distributed temperature sensing optical cable, the NLIW transformations were observed from 2000 to 2 m on the flanks of Dongsha Atoll (Pratas Reef). Possible outcomes included reflection, refraction around the island, wave breaking, and penetration into shallow water. Upslope penetration depended on incident wave amplitude and direction as well as the local stratification.

Plain Language Summary Because the ocean is stratified, it supports a wide range of internal waves in addition to the surface waves we observe all the time. Some of the largest such waves in the world, taller than the Washington Monument, are generated between Taiwan and the Philippines when the tide crashes into the underwater ridge system in the Luzon Strait. These "internal tides" continue to grow and steepen as they propagate west northwest across the South China Sea and eventually break forming the high frequency waves reported here. The waves are transformed as they enter shallower water surrounding a tropical reef, often splitting to form packets and ultimately breaking on the bottom much like surface waves do. Vertical currents surrounding the waves pump nutrients from the depths to the surface, nourishing the reef. The fate of the wave energy is complex and may be reflected, refracted, or dissipated on the reef.

1. Introduction

Several large research programs have been conducted in the northeastern South China Sea since 2001 to study the world's largest nonlinear internal waves (NLIWs) as they are generated in the Luzon Strait, propagate west-northwest across the sea, and shoal on the Chinese continental slope and shelf (Alford et al., 2010, 2015; Farmer et al., 2011; Lien et al., 2014; Ramp et al., 2010, 2019). The final piece of the story, in which the waves reverse polarity in water less than roughly 100–150 m depth (Fu et al., 2012; Liu et al., 2004; Orr & Mignerey, 2003; Ramp, Chiu, Kim, et al., 2004) and ultimately dissipate in shallow water, have remained largely unstudied in situ as it takes place over the heavily fished continental shelf. Dongsha Atoll is a remnant caldera rising 500 m from the ocean floor (the Dongsha Plateau) to the sea surface (Figure 1) and its location presents the opportunity to study a wide variety of shoaling phenomena. Satellite remote sensing shows several possible outcomes for incident NLIWs: Some are modified by significant reflection from the reef (Bai et al., 2017), some are refracted around the reef forming complex patterns behind it (Hsu & Liu, 2000; Li et al., 2013; Liu et al., 2004; Jackson, 2009; Jia et al., 2018; Zhao et al., 2008), and some pass by it with seemingly little change of form. Theoretical work suggests that the shoaling NLIWs may continue to propagate upslope adiabatically, form packets via dispersive tails, or break, depending on the ambient stratification, bottom slope, and the amplitude of the incident wave (Lamb & Warn-Varnas, 2015; Small, 2001a, b; Vlasenko & Hutter, 2002; Vlasenko & Stashchuk, 2007). When the wave's orbital velocity exceeds the propagation speed, usually between 300 and 150m depth, the largest waves may break and form trapped cores that transport mass and nutrients onshore (Chang, Cheng, et al., 2021; Farmer et al., 2011; Lien et al., 2012, 2014). Still farther onshore where the upper layer thickness exceeds the

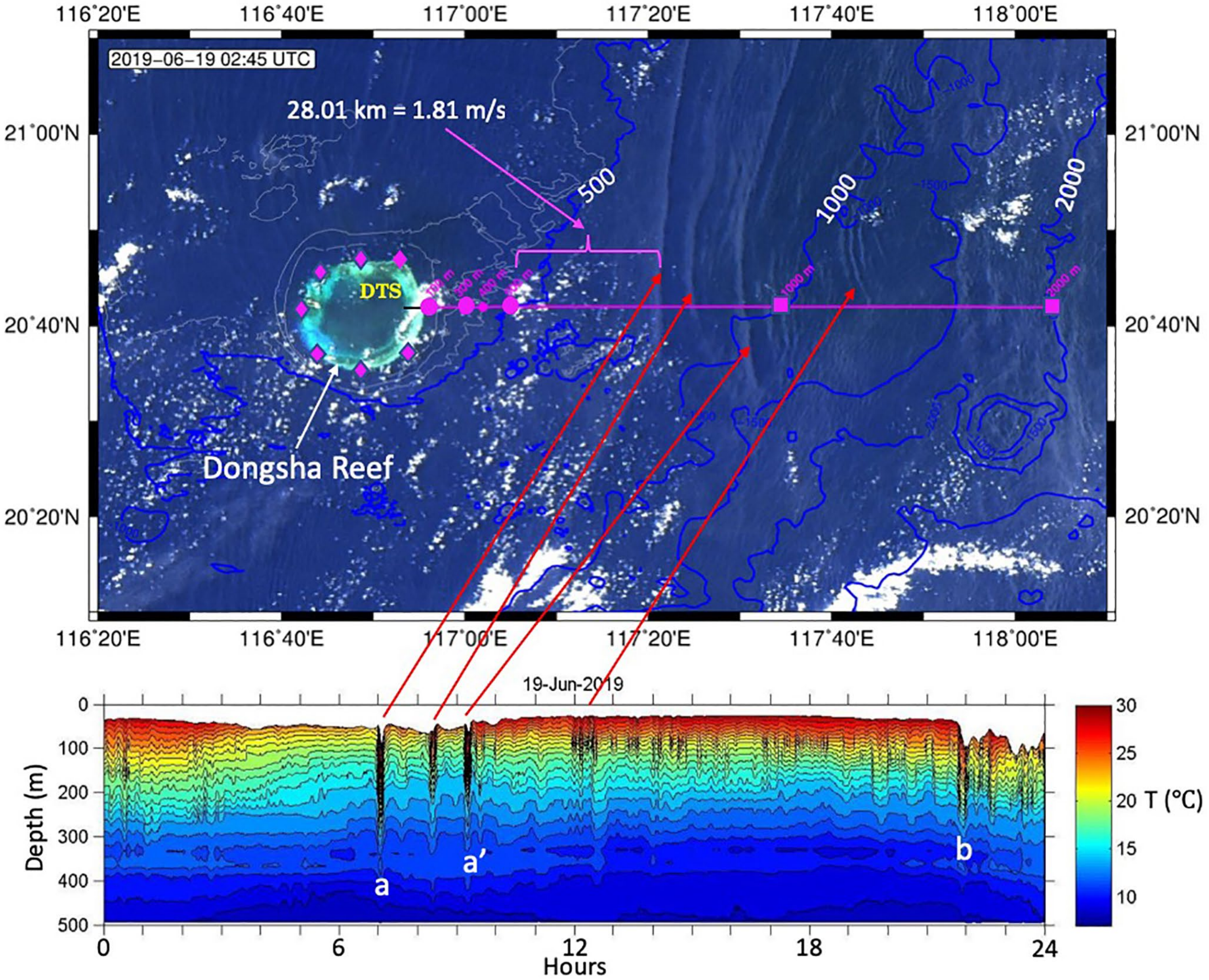

Figure 1. Locator map and introduction to the phenomena studied during the Dongsha Reef nonlinear internal waves field experiment. Deep-water inverted echo sounders with pressure sensors are designated by magenta squares and T/C/P moorings by magenta circles. The magenta diamonds surrounding the reef indicate the locations of temperature and velocity observations at approximately 25 m deep. The distributed temperature sensing cable location extending from 2 to 50 m is shown by the solid black line. The horizontal scale of the incoming waves is clearly seen in the Moderate Resolution Imaging Spectroradiometer ocean color image from 19 June 2019 (top panel) in the background. The wave signatures in ocean temperature as they pass the 500 m mooring, shown in the panel below, demonstrate the remarkable fidelity with which the satellite imagery resolves the details of the features beneath. The elapsed time between the image and the mooring passage can be used to compute the wave propagation speeds. Note the b-wave in the lower panel has not yet entered the field of view in the image.

lower, the depression waves are transformed into elevation waves (Duda et al., 2004; Liu et al., 2004; Orr & Mignerey, 2003; Ramp, Chiu, Kim, et al., 2004). The elevation waves presumably continue propagating west northwest (WNW) toward shore and dissipate in shallow water, but observations to the west of this point are scarce.

Two types of NLIWs, called a-waves and b-waves, have been repeatedly observed, parlance first coined by Ramp, Chiu, Kim et al. (2004). The distinction matters since the initial conditions for wave generation must be understood to understand the observed wave arrival patterns in the western SCS and to improve numerical forecasting of wave arrivals and characteristics. Several conflicting ideas about wave generation have been advanced over the years (Alford et al., 2010; Chen et al., 2013; Du et al., 2008; Ramp et al., 2010; Vlasenko et al., 2012). Most recently, using the first truly three-dimensional observing network between the Luzon Strait and the Chinese continental shelf, Ramp et al. (2019) determined that the a-waves were generated in the southern portion of the strait and the b-waves to the north, in agreement with the three-dimensional modeling results of Zhang et al. (2011). An important factor that accounts for most of the wave differences downstream is that the b-waves are subject to massive dissipation over the shallow northern portion of the western (Heng-Chun) ridge (Alford et al., 2011) but the a-waves are not. The geometry combined with a detailed knowledge of the barotropic tide in the strait accounts for most of the observed differences between the two types of waves. The subject is revisited further for these new observations in the results section.

Earlier studies (Fu et al., 2012; Lien et al., 2014; Yang et al., 2004) observed the NLIW energies offshore of the 100 m isobath near Dongsha but had no observations toward the reef. Reid et al. (2019) and Davis et al. (2020) had observations on the reef but no observations of the incident energies offshore. The overall goal of this project is to use moorings and shipboard observations to track the waves all the way from the 2,000 m isobath to the reef crest and determine which waves most efficiently transfer momentum and buoyancy up the slope surrounding a subtropical atoll. The subject is important because the acoustic transmission (Chiu et al., 2004, 2013; Duda et al., 2004; Ramp, Chiu, Bahr, et al., 2004; Reeder, Chiu, & Chen, 2010), sediment resuspension (Aghsaee & Boegman, 2015; Bogucki et al., 2005; Diamessis & Redekopp, 2006; Reeder, Ma, & Yang, 2010; Stastna & Lamb, 2008) and nutrient supply to the reef via upwelling and cross-shelf exchange (Reid et al., 2019; Wang et al., 2007) all depend on the shoaling nonlinear internal waves. Additionally, marine operations in the vicinity of the reef involving divers and/or small autonomous vehicles are effectively prohibited when the strong currents and buoyancy fluctuations induced by the waves are present. More specifically, the overall project intends to:

- Describe the nature and variability of the incident wave field impinging on the atoll from the Luzon Strait as the waves shoal through the array
- Describe shoaling, breaking, and internal run-up onto the reef to determine which waves and stratifications are most amenable to upslope penetration
- Examine the details of wave breaking and turbulent dissipation (Chang, Cheng, et al., 2021)
- Study reflection from and refraction around the reef using satellite remote sensing and a ring of temperature and velocity observations in shallow water around the reef
- Observe the impact of the wave field surrounding the reef on acoustic propagation
- Use the observational data in conjunction with the Navy's Luzon Strait Nowcast/Forecast System (LZSNFS) (Chen et al., 2013; Rogers et al., 2019) to predict the NLIW structures and arrival times in the northeastern South China Sea

By describing the nature of the incident wave field in detail, this paper sets the stage for other papers to follow. The emphasis is on understanding the NLIW arrival patterns and transformations due to the shoaling bottom and ever-changing local stratification in the region between the 2,000 m and 100 m isobaths. A few ideas regarding the region inshore of 100 m are introduced. A companion paper emphasizes the wave transformation processes in very shallow water onshore of the 100 m isobath where elevation waves and upslope-propagating bores are formed (Sinnett et al., 2021). Subsequent papers focusing on the numerical modeling and acoustic implications of the shoaling NLIWs will be forthcoming.

2. Data and Methods

The field experiment was conducted from May 14 to 27 June 2019 focusing on an east/west transect along roughly 20° 42'N extending from 118° 04.3'E (2,000 m) to 116° 55.4'E (10 m; Figure 1, Table 1). The transect consisted of three sections: At 1,000 m and 2,000 m, inverted echo sounders with pressure sensors (PIES) were mounted on the bottom looking up. PIES sample the round-trip travel time for a 12-kHz acoustic ping from the bottom to the surface and back. Nonlinear internal waves can be clearly sensed by the instruments due to their very large perturbations of the main thermocline which in turn alter the acoustic travel time. Via extensive comparisons with moored observations, the PIES have been shown to do a good job of sampling nonlinear wave amplitude and time of passage (Li et al., 2009). While the units are not sensitive to higher mode waves, this was not a problem in deep water where almost all the NLIWs were mode one depression waves (a downward displacement of the thermocline). The sampling rate of 16 pings burst-sampled every 10 min was not as fast as the moorings but were sufficient to show the form and timing of the incoming waves while they were still evolving nonlinearly in deep water before interacting with the bottom.

The next section of the transect nearer to the atoll consisted of subsurface oceanographic moorings deployed at the 500, 300, 100, 50, 20, and 10 m isobaths. Separate moorings were used for temperature and velocity at some

Table 1
Mooring and Instrument Locations and Performance

Mooring name	Latitude (north)	Longitude (east)	Bottom depth (m)	Instrument	Instrument depth (m)	Start	Stop	Record length (d)	Sample interval (s)
PIES2000	20 41.837	118 04.323	2,025	PIES	2,025	19/05/2019	22/06/2019	33	37
PIES1000	20 42.270	117 35.542	1,017	PIES	1,017	19/05/2019	22/06/2019	33	37
500 A	20 42.136	117 05.076	512			15/05/2019	23/06/2019	39	
				[c]ADCP 75 kHz	511		No Data		
				[b]ADCP 300 kHz	511				60
				MAVS	511				60
				SBE 39 (TP)	511				60
500T	20 41.983	117 04.985	505			15/05/2019	23/06/2019	39	
				S70	34, 122, 212				60
				S7p, S7t	242				60
				SBE 39 (TP)	422, 493				60
				SBE 56 (T)	63, 93, 153, 183, 242, 273, 333, 363, 392, 483				60
BPTR	20 41.923	117 01.929	400	TP	400	17/05/2019	22/05/2019	4	2
300 A	20 41.759	117 00.059	320			15/05/2019	22/06/2019	38	
				[c]ADCP 75 kHz	321				6
				[a]ADCP 600 kHz	321				60
				MAVS	321				60
				SBE 39 (TP)	321				60
300T1	20 41.689	116 59.934	323			14/05/2019	22/05/2019	9	
				SBE 56 (T)					10
				SBE 39 (T&TP)	} Every 5 m, 26–268 m				10
300T2	20 41.759	116 59.806	313			23/05/2019	22/06/2019	30	
				Hydrophone	25	23/05/2019	22/06/2019	30	13.7 kHz
				S9	32, 154, 248				60
				SPE 56 (T)	62, 93, 124, 186, 217, 278				60
100A	20 41.624	116 56.208	100			14/05/2019	22/06/2019	38	
				[b]ADCP 300 kHz	100				60
				MAVS	100				
				SBE 39 (TP)	100				60
100T	20 41.700	116 56.141	92			14/05/2019	22/06/2019	38	
				SBE 39 (TP)	20, 52				60
				SBE 56	36, 67				60
				S9	82				60

Table 1
Continued

Mooring name	Latitude (north)	Longitude (east)	Bottom depth (m)	Instrument	Instrument depth (m)	Start	Stop	Record length (d)	Sample interval (s)
50 m	20 41.965	116 55.806	51			16/05/2019	12/06/2019	28	
				ADCP 600 kHz	48				1
				SBE 37 (CTD)	8, 48				60
				SBE 56 (T)	Every 2.5 m, 10–48 m				1
20 m	20 41.966	116 55.511	21			16/05/2019	11/06/2019	27	
				ADCP Sentinel V	21				1
				SBE 39 (TP)	6				10
				SBE 56 (T)	Every 1.5 m, 8–20 m				1
10 m	20 41.987	116 55.421	12			16/05/2019	12/06/2019	28	
				ADCP 600 kHz	10				1
				SBE 37 (CTD)	4				60
				SBE 56 (T)	Every 1.5, 4–12 m				10
DTS			0–50	T	5 km cable every 0.25 m	16/05/2019	12/06/2019	28	23

[a] 2-m bins up-looking, 30 2-s pings per ensemble. [b] 4-m bins up-looking, 30 2-s pings per ensemble. [c] 8-m bins up-looking, 6 1-s pings per ensemble.
Abbreviation: ADCP, acoustic Doppler current.

sites to minimize the impact of mooring blow-down by strong currents. Temperature, salinity, and pressure were sampled by a combination of T, TP, and TCP type instruments sampling at 1 s to 1 min intervals (Table 1). All had sufficient temporal resolution to make un-aliased observations of the passing internal waves. Currents were sensed by acoustic Doppler current profiler (ADCP)-type instruments with varying operating frequencies, depending on the range needed to cover a particular water depth. These instruments typically grouped 1 s pings into 1 min ensembles. Final velocities in earth coordinates were produced in post-processing.

For a subset of the mooring deployment (May 14-22) a high-resolution temperature string was additionally deployed at the 300 m isobath (20° 41.69'N, 116° 59.93'E). This mooring had temperature sensors deployed every 5 m from 5 to 250 m sampling at 10 s intervals (Table 1, 300T1). The high-resolution array was primarily used in conjunction with the shipboard data to study wave breaking and turbulent dissipation (Chang, Cheng, et al., 2021). The T-string was replaced by a more modest seven-instrument array sampling at 1 min intervals for the May 23 – June 22.

Finally, the portion of the transect from the reef crest to 50 m depth was sampled using a 5-km long distributed temperature sensing (DTS) optical cable laid out along the bottom. Laser light was pulsed along the cable and the ratio of Stokes to anti-Stokes laser backscatter intensity was related to the cable temperature at locations determined from time-of-flight observations. The cable was assumed to be in thermal equilibrium with the water and had a response time of about 12 s (Sinnett et al., 2020). DTS derived temperature observations thus obtained were calibrated following Sinnett et al. (2020) to estimate water temperature with <0.2°C RMSE at 23 s temporal and 0.25 m spatial resolution. These nearly continuous (in time and cross-shore distance) DTS temperature observations provided unique insight into the internal runup of the incident wave field.

The ring of magenta diamonds depicted in Figure 1 shows seven temperature sensors and two ADCPs deployed between 10 and 25 m depth around the reef to obtain in situ observations of refracted waves for comparison with satellite remote sensing. These are the first in situ observations of wave refraction around the reef and will provide a much more complete picture of the phenomenon than the highly intermittent satellite data. A subsequent manuscript will be dedicated to the analysis of these time series within the context of the internal wave environment presented in this paper.

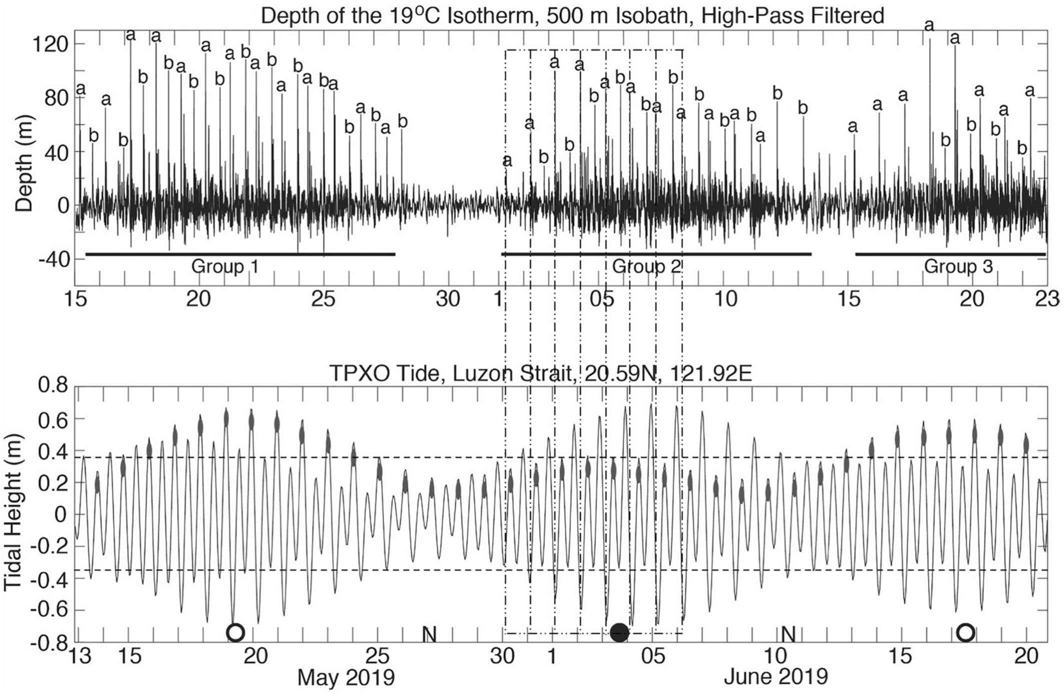

Figure 2. (Top) Time series showing the depth of the 19°C isotherm observed by the mooring located at the 500 m isobath (Figure 1). The time series was high pass filtered to separate thermal displacements due to NLIWs from the internal tides and mean (mesoscale and seasonal) flows. The sharp depressions of the isotherm indicate passing NLIWs. (Bottom) Tidal amplitude in the central Luzon Strait from the TPXO global tidal model (Egbert & Erofeeva, 2002), at a point located between Batan and Itbayat Island in the Luzon Strait. Open circles indicate full moons, filled circles new moons, and N = neap tide. The waves (top panel) have been lagged back by the propagation time (51.6 hr) to better align with the barotropic tidal envelope in the generating region. The dot/dashed vertical grid shows that the a-waves aligned precisely with the ebb tide at this lag. The horizontal dashed lines indicate the approximate tidal amplitude needed for wave generation. The dark gray ellipses show that the major and minor tidal beats switched places during the neap tides.

3. Results

3.1. Characteristics of the Incident Waves

The displacement of the 19°C isotherm at the 500m isobath is used here as an indicator of the incident wave arrival patterns on the continental slope before they interact too much with the bottom (Figure 2). This isotherm was chosen because it rarely intersected the surface or bottom, was near the nodal point of the waves (120–140 m), and was relatively smooth and free of small undulations due to instabilities and mixing. The time series was high-pass filtered with a cutoff period of 5.9 hr to separate the NLIW displacements from others due to the tidal and mesoscale variability (Ramp, Chiu, Kim, et al., 2004). The computed displacements are within a few meters of those computed using the 18°C isotherm by Chang, Cheng et al. (2021). The choice is not critical for the purpose of tracking amplitude changes as the waves propagate shoreward.

A total of 73 wave arrivals with amplitude greater than 30 m (as determined by the high pass filtered, zero-mean 19°C isotherm displacement) were observed that show a pattern of wave amplitudes modulated by the fortnightly tidal cycle (Figure 2, top). Three fortnightly (14-day) cycles were observed: the largest waves exceeded 100 m in amplitude near spring tide and no waves were observed around the neap tide. Type a- and type b-waves can be easily identified via their arrival times, packet structure, and propagation direction which results from the b-waves being generated in the northern Luzon Strait and the a-waves in the south (Du et al., 2008; Ramp et al., 2019; Zhang et al., 2011). Generally speaking, one of each type of wave arrived each day with the b-waves leading the a-waves by about 10 hr, but the exact time difference was a function of wave position within the fortnightly cycle (see also Figure 3).

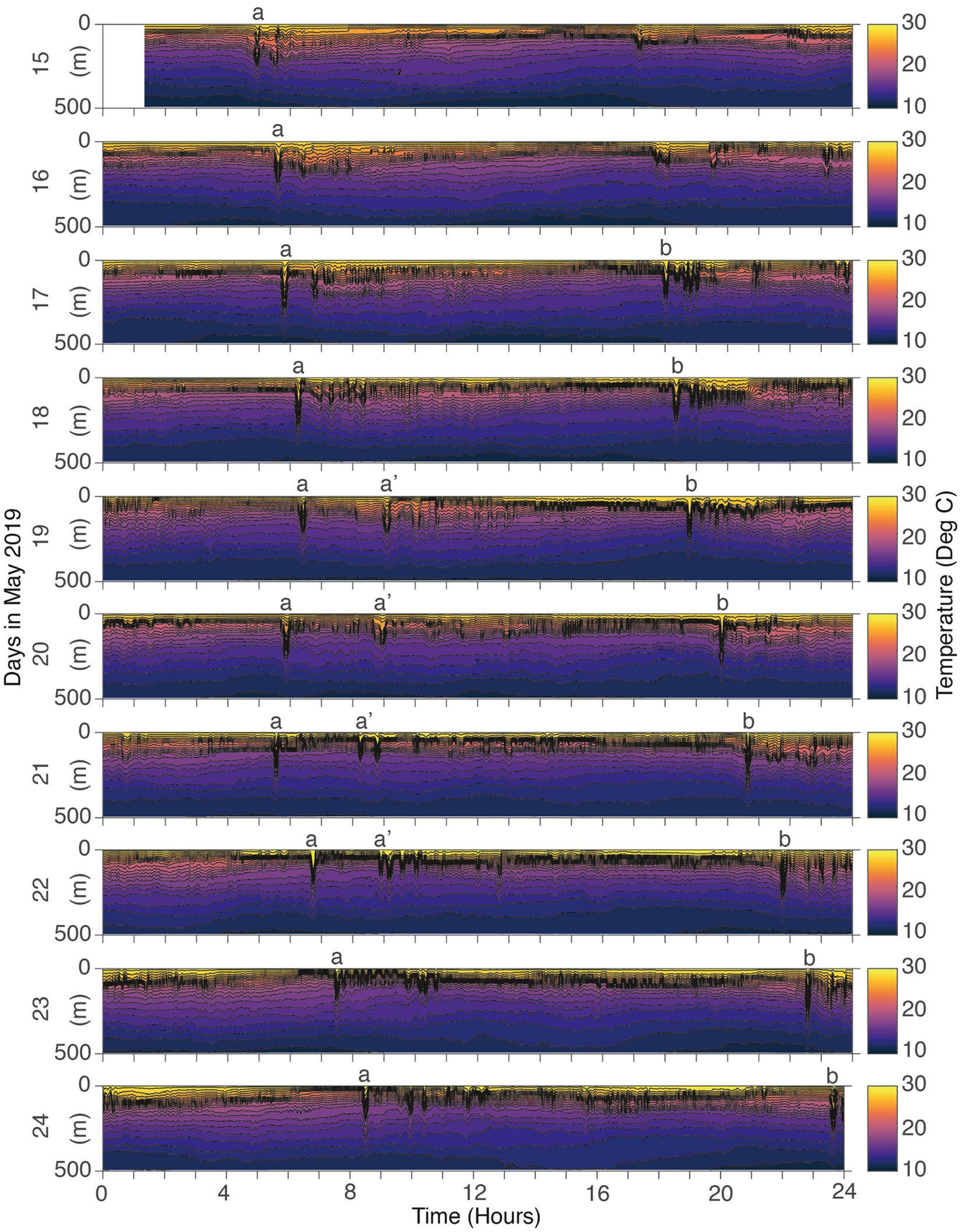

Figure 3. Temperature contours at the 500 m isobath during May 15-24, 2019 showing the temporal evolution of wave arrival patterns at that point. These waves are from Group 1 (Figure 2) but have many characteristics in common with the wave arrivals in groups 2 and 3.

While tracing wave origins was not the point of this experiment, it can be inferred from a more complete trans-basin data set located just to the north of the Dongsha transect (Ramp et al., 2010) that the waves required on average 51.6 hr to cross the basin from the generation sites in the Luzon Strait to the T500 location. Thus, the local fortnightly envelope of NLIW arrivals lagged the pattern of the barotropic tides in the Luzon Strait (Figure 2, bottom) by about this amount. Only the major beats of the diurnal inequality generated waves: the minor beats (and the beats at neap tide) lacked sufficient excursion across the generating topography to produce NLIWs. Not all fortnights were the same: Group 2 had slightly smaller waves than groups 1 and 3. Group 3 had a distinct lack of type-b waves. A few small waves persisted during the neap tide between groups 2 and 3, due to an anomalously strong neap tide in the Luzon Strait. Recall that the waves have already traveled 500 km over 51 hr to reach the point of observation. These differences between fortnights are attributed to changes in stratification, wind stress, and mesoscale variability along the propagation path (Du et al., 2008; Li et al., 2016; Park & Farmer, 2013), in addition to the variability of the barotropic tide at the generation sites.

An expanded view of the Group 1 waves shows an example of the temporal variability of wave arrivals in more detail (Figure 3). May 15 marks the beginning of the cycle when waves were just starting to arrive following the previous neap tide. The first a-waves on May 15 and 16 were relatively small and began arriving earlier in the fortnightly cycle than the b-waves. The a-waves consisted of two-wave packets from the very beginning. The a-waves remain larger than the b-waves through May 19, but the waves were subsequently similar in amplitude on May 20 and the b-waves became larger during May 21-24. The a-waves arrived daily around 0600 through May 21 but then started arriving an hour later each day from May 21-24. The b-waves arrived roughly an hour later each day throughout. Due to this phenomenon, the b-wave arrivals became closer in time to the a-waves as the fortnightly cycle progressed. Both types of waves were generated diurnally. The local wave arrivals only appeared to be semidiurnal since they were coming from different locations in the Luzon Strait. Upon close inspection, they were not quite semidiurnal.

During May 19-22, a second large wave (the a′ wave) appeared about two hours after the primary a-wave. This wave was only generated when the source forcing was large (near spring tide) and presumably comes from a third source located near the a-wave source in the southern Luzon Strait (Ramp et al., 2019). It was similar in amplitude to the a-wave (sometimes even larger) and was too far behind it to be part of the same packet. Per the example in the Moderate Resolution Imaging Spectroradiometer image (Figure 1), the along-crest extent is similar to the a-wave whereas packets tend to be more localized. As the source forcing continued to weaken on May 23-24, the a-wave structure was again similar to May 16-17 when the remote tidal forcing was comparable.

3.2. Spatial transformation under shoaling

The incoming NLIWs were first detected by the PIES on the 2,000 m isobath (Figure 4). Two subsets of the data are shown for illustration, a period of waxing tide from June 17-22 and waning tide from May 21-25. In both cases, the b-waves originated from very sharp depressions of the internal tide, also known as “corner waves” (Helfrich & Grimshaw, 2008; Li & Farmer, 2011). The corner waves most commonly evolved into a single solitary wave at T500, as per Figure 4d, but sometimes formed two waves during stronger forcing, for example, May 21 (Figures 4a and 4b). As mentioned previously, the b-waves became much larger and more vigorous during the second half of the fortnightly envelope (compare Figures 4b and 4d). The reason for this is not completely clear but may be due to a relatively more vigorous semidiurnal tidal component as the neap tide is approached (Li & Farmer, 2011). During weaker forcing (not shown) the corner waves were rounded and produced no NLIWs downstream. The a-waves by contrast originated from a series of two and sometimes three oscillations about 10 hours into the tidal displacement at 2,000 m (Figures 4a and 4c). These oscillations consistently evolved into two or three-wave packets at T500, whose amplitude tracked the strength of the tidal forcing. The mean propagation speed for all the waves between PIES2000 and T500 was about 2.6 m s^{-1}.

The PIES2000 observations were similar to previous PIES observations nearby. Two instruments were deployed during 2005 and 2007 at a site located 92 km to the northeast on the 2500 m isobath (Li et al., 2009; Li & Farmer, 2011). A similar instrument was deployed during July – December 2011 at a site located 76 km due east at 2,682 m depth (Ramp et al., 2019). The PIES2000 observations were most similar to the longer time series during times when the forcing was mixed diurnal/semidiurnal as was the case here.

Stack plots of four representative shoaling events are presented to show how the waves changed from the 500m isobath to the reef crest (Figure 5). The examples were chosen to show how the thermal structure changed for strong waves, weaker waves, and no waves as they propagated upslope toward the reef. On May 17 (Figure 5a) the a-waves decreased in amplitude from 122 to 93 m from the 500–300 m isobath and the b-waves remained about the same (89–92 m). The propagation speed was 1.78 m s^{-1} for the a-wave versus 2.03 m s^{-1} for the b-wave.

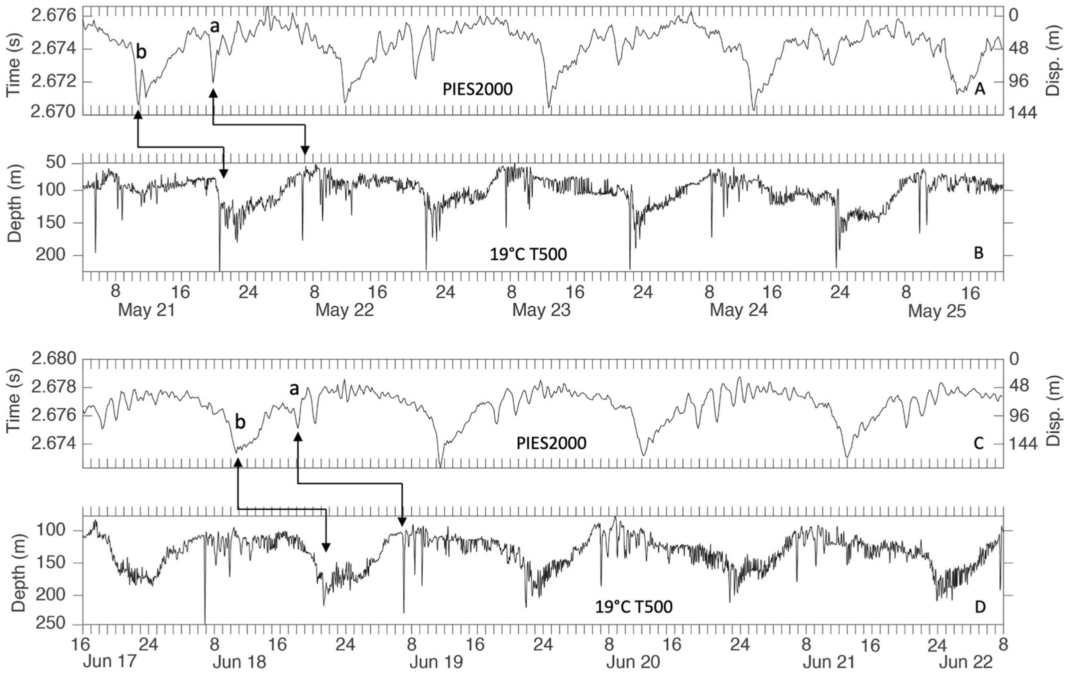

Figure 4. Acoustic travel time at PIES2000 over the depth of the 19°C isotherm at 500 m for May 21–25, 2019 (a), (b) and June 17–22, 2019 (c), (d). A travel time change of 0.001 s corresponds to a thermocline displacement of 24 m. The corresponding displacement in meters is shown on the right-hand *y*-axis for convenience.

Continuing upslope, the waves were still discernible but much less clear at the 100 m isobath. The propagation speed slowed to 0.98 m s^{-1} for the a-wave and 1.17 m s^{-1} for the b-wave. Inshore from 50 m, the b-wave took the form of a broad warm front (Figures 5a, 1900-2100). This feature results from the surface part of the wave traveling faster (arriving earlier) than the bottom and was notably less prominent for the a-waves. Another noteworthy feature in the May 17 sequence was the active splitting of the b-wave into a nine-wave packet between 500 and 300 m (Figure 5a, time = 1900). The trailing waves in the packet were about equal in amplitude and were evenly spaced, unlike the rank-ordered two-wave a-wave packet which was already present at 500 m. The new b-wave packet is attributed to shoaling and is described further in the discussion section. In the May 17 example and in fact, all four examples have shown, the wave splitting and the sloping wave front were more commonly associated with the b-waves than the a-waves. This would seem to indicate that the b-waves were interacting more strongly with the bottom than the a-waves.

The incident NLIWs at 500 m on May 19 remained large but were slightly smaller than on May 17. The a-wave grew in amplitude from 97 to 107 m while the b-wave shrank from 85 to 69 m between the 500 and 300 m isobaths. Propagation speeds varied little across this depth range throughout the experiment, with mean values of 1.76 m s^{-1} and 1.91 m s^{-1} for the a-waves and b-waves respectively. This is a puzzling result since larger NLIWs are expected to travel faster due to the nonlinear contribution to the phase speed. The reasons for the observed outcome are revisited below in the discussion section. The feature of interest on May 19 was the formation of an elevation wave behind the b-wave at 100 m and shoreward. When elevation waves formed, they were quite persistent and could be clearly seen at 50 m and even at 20 m, in this case, centered near 2200 hr (Figure 5b). The criterium used for acceptance as an elevation wave is that the wave polarity (vorticity) be reversed with respect to the leading depression wave (Shroyer et al., 2009). For the waves near Dongsha, this means that the elevation waves have ESE (offshore) velocity in the upper layer and WNW (upslope) velocity in the lower layer, with upwelling ahead of the wave and downwelling behind. By this criterium, only 19 out of 73 incident depression waves produced elevation waves closer to shore. The reasons for this unexpected result are explored further below.

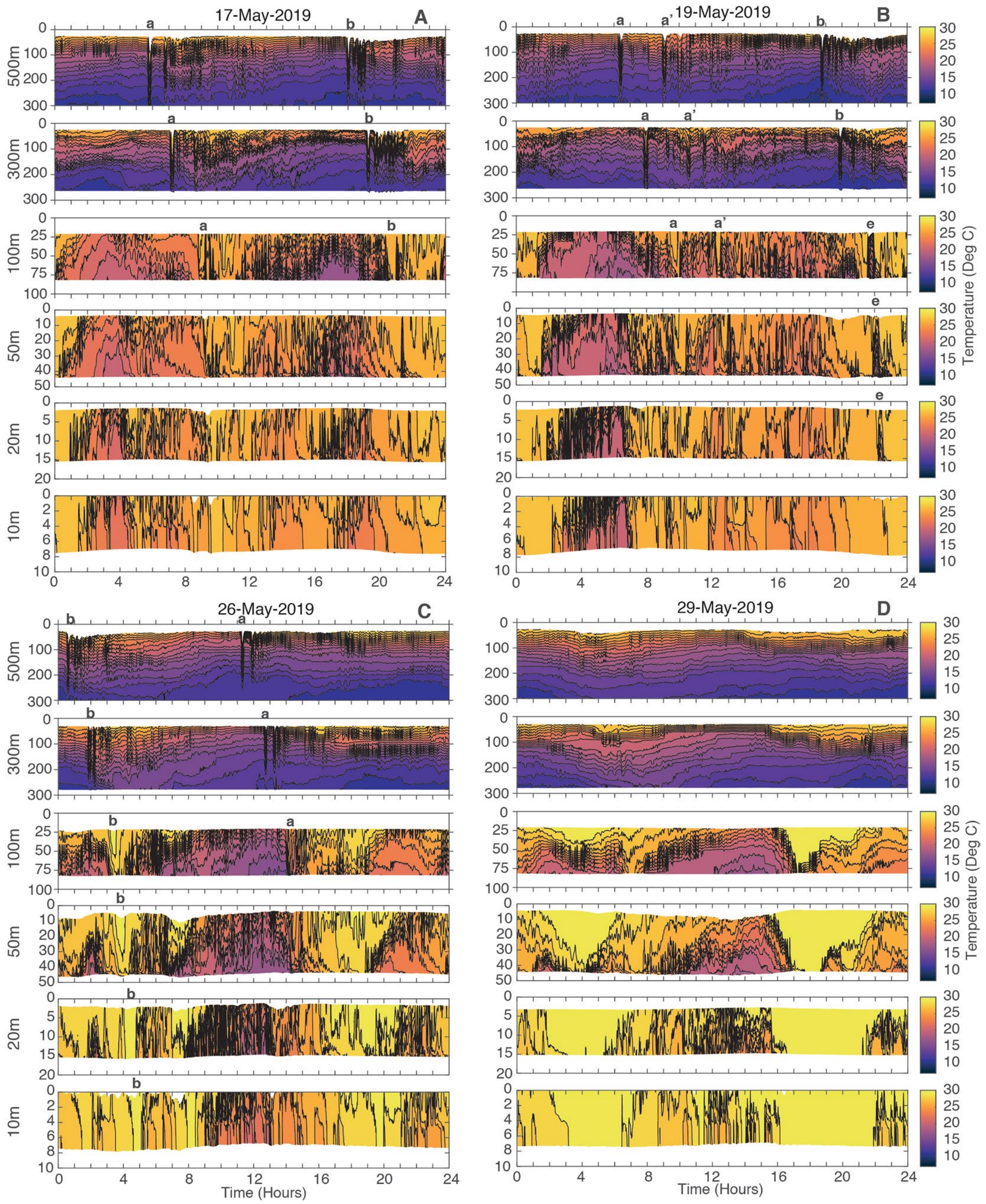

Figure 5. Four examples of nonlinear internal solitary waves (NLIWs) shoaling from the 500 m to the 10 m isobath. (a) May 17, strong waves with b-wave packet formation; (b) May 19, strong waves with elevation wave; (c) May 26, weak waves; (d) May 29, no NLIWs. The color palette is uniform to facilitate comparison but the vertical scale changes to show the wave structure. Note the scale for the 500 m isobath was chosen to match 300 m (the bottom 200 m is not shown). Type a- and b-waves are labeled accordingly. The "e" at around 2200 hr on May 19 indicates an elevation wave.

A particularly good example from May 18 shows how the velocity structure evolved between the 300 and 100 m isobaths (Figure 6). The wave-induced horizontal velocity in the lower layer changed from 60 cm s^{-1} downslope at 300 m to 60 cm s^{-1} upslope at 100 m. The vertical velocities, at $\pm$ 40 cm s^{-1} were among the highest observed anywhere in the ocean. The vertical velocities produce upwelling behind the wave in deep water but ahead of the wave at 100 m. The vorticity was positive in the depression wave and negative in the elevation wave. These velocities, combined with a flow separation point in the bottom boundary layer near 1930 hr, lift massive

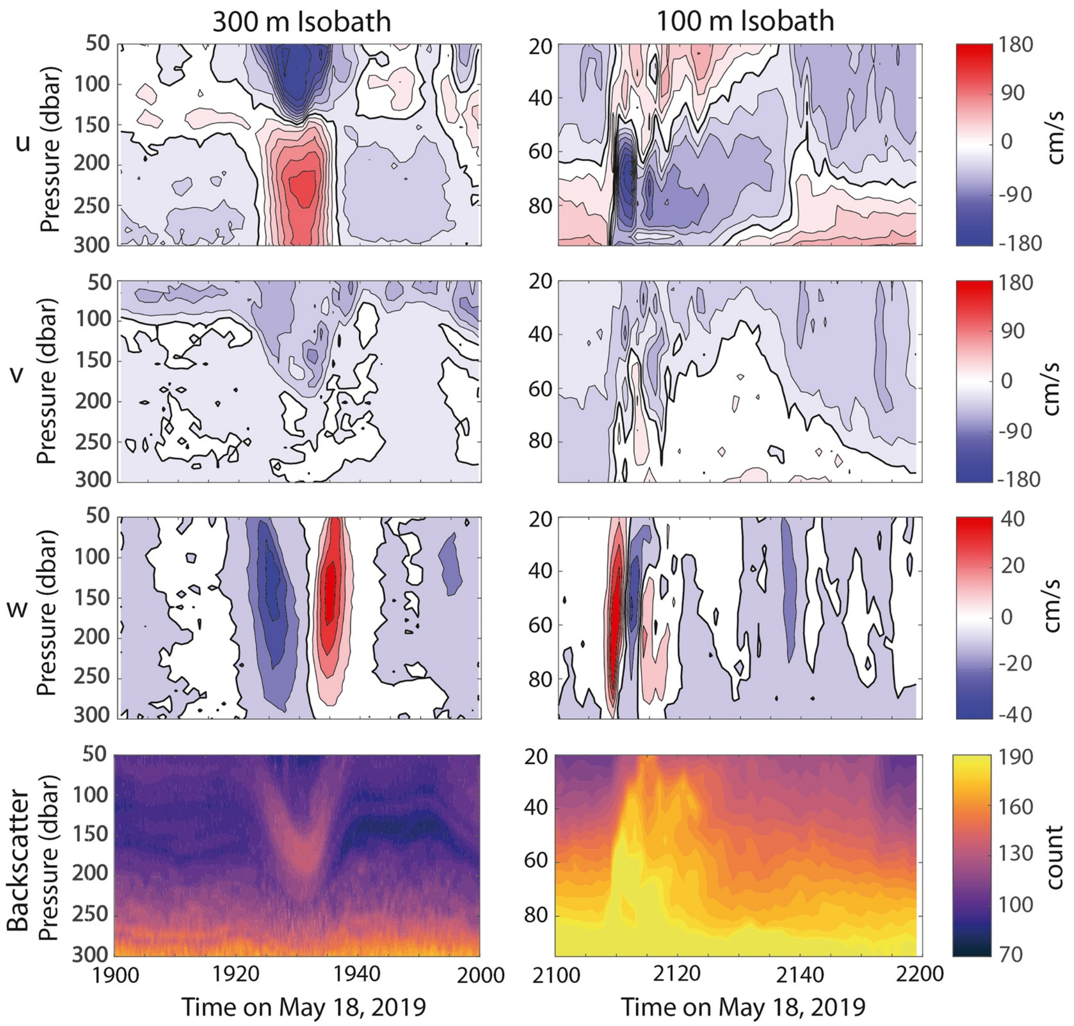

Figure 6. An example of an incoming depression wave at the 300 m isobath transforming into an elevation wave at the 100 m isobath on 18 May 2019. The velocities are 1-min averages from an acoustic Doppler current profiler (ADCP) sampling at 1-s intervals. Positive velocities are eastward, northward, and upward for u, v, and w respectively. Both waves propagate west-northwest (upslope) driving downslope bottom currents under the depression wave but upslope under the elevation wave. The "backscatter" is the echo intensity from beam-3 of the ADCP. The echo from organic particulates in the water column in the depression wave (left panel) was much weaker than from resuspended sediments under the elevation wave (right panel).

amounts of sediment into the water column as the wave passes (Figure 6, bottom). This was a common feature of all the elevation waves observed. The total onshore energy flux (kinetic, potential, and perturbation pressure) has been calculated using these same data for a variety of wave types and ambient background conditions (Sinnett et al., 2021). This particular wave retained 14.6% of its total energy flux as it propagated from 300 to 100 m and transitioned into an elevation wave. The lost energy is attributed to very high turbulent kinetic energy (TKE) dissipation (10^{-6} – 10^{-4} W kg^{-1}) along the propagation path due to both convective and Kelvin-Helmholtz instability (Chang, 2021; Chang, Cheng, et al., 2021). Despite being weakened, the elevation waves were likely important in the shoreward transport of mass and heat in that the elevation waves persisted farther upslope than the depression waves, which all disintegrated by the 50 m isobath.

An expanded view of the combined velocity and temperature structure including the DTS cable for the May 19 shoaling b-wave event (Figure 5b) shows the extreme upslope penetration of the elevation wave (Figure 7). The event began as a large depression wave at the 300 m isobath (Figure 7a) with westward (upslope) velocity in the surface layer and downslope flow below. By the time it reached 100 m however, the depression wave had weakened and broadened, and the trailing elevation wave had become the strongest feature (Figure 7b, top panel).

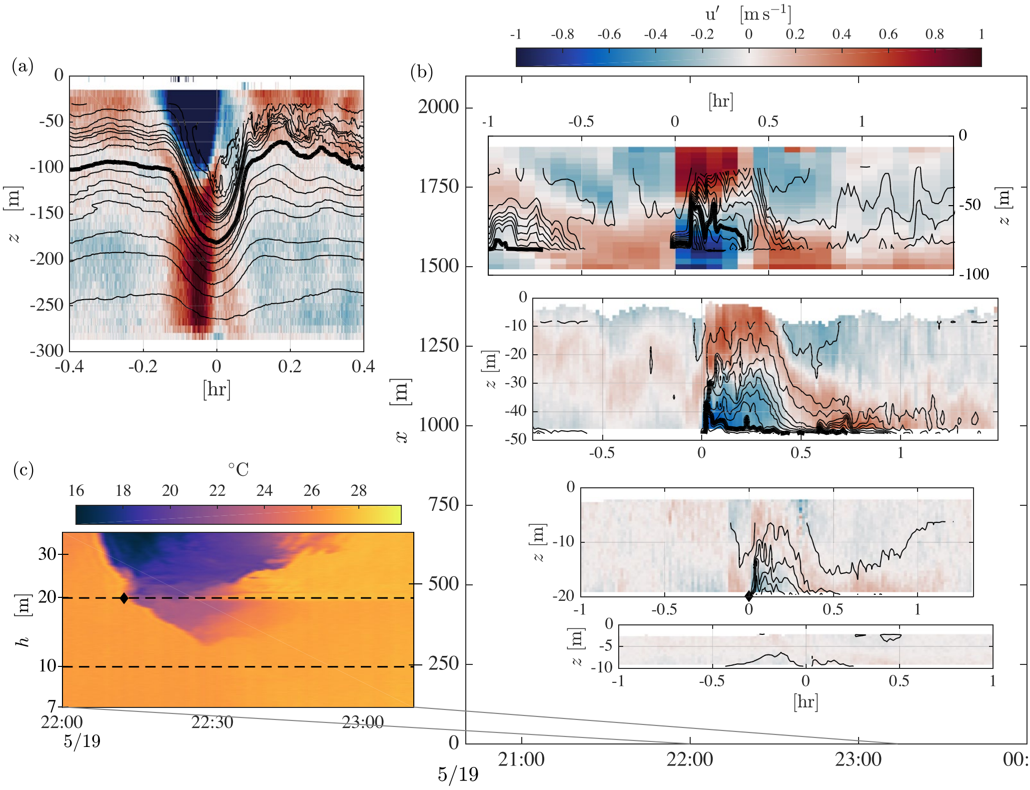

Figure 7. (a) Combined velocity and temperature for the incident depression wave shown at 1900 hr on May 19 (Figure 5b). Temperature contours are drawn every 1°C with the 19°C contour in bold. (b) Combined velocity and temperature from the 100 m, 50 m, 20 m, and 10 m isobath showing the evolution of the elevation wave trailing the initial depression wave. (c) Bottom temperature from the distributed temperature sensing cable. The cable was deployed along the same onshore/offshore transect as the moorings and is offset here for clarity. The 10 and 20 m isobaths are indicated by the horizontal dotted lines. Note that the bottom slope was not linear, and (h) represents the bottom depth while (z) represents depth in the water column.

The elevation wave clearly displays the reversed polarity described above. The feature remained equally clear at 50 m (Figure 7b), and while the velocities weakened, the elevated thermal structure due to the upslope cold surge remained evident at the 20 m isobath as well. The DTS cable shows that the upslope cold surge transported water as much as 10°C colder than ambient (16°C vs. 26°C, Figure 7c) up the forereef slope. There was no indication of upslope transport by the remnants of the initial depression wave, thus the elevation waves appear to be quite important to the reef-nourishing process. The transformation of elevation waves into upslope internal bores on the reef flank is described in greater detail in Sinnett et al. (2021).

The sequence from 26 May 2019 shows the upslope evolution of somewhat smaller NLIWs (Figure 5c). These waves evolved from weaker source forcing as the neap tide was approached (Figure 2). The wave amplitudes between the 500 and 300 m isobaths increased slightly for the a-waves (67–80 m) and remained about the same (50 m) for the b-waves. Note that by virtue of arriving an hour later each day, the b-waves arriving around 1900 hr on May 19 now arrived at around 0030 on the 26th. These waves, especially the b-waves, retained their form better in shallow water than the larger waves and could be easily tracked all the way to the 10 m isobath. This was not surprising since all else being the same, smaller amplitude NLIWs will progress farther up a slope before breaking than larger waves (Lamb & Warn-Varnas, 2015).

Finally, it is instructive to show a sequence corresponding to neap tide in the Luzon Strait at a time when no NLIWs were observed along the Dongsha transects (Figure 5d). This example shows that the primary mechanism driving temporal changes to the ambient stratification at the Dongsha site was the local internal tide. At certain times for instance 0400 hr at the 100 m isobath, the thermocline was very close to the bottom and the upper layer thickness h_1 was clearly greater than the lower layer thickness h_2. Later, around 1400 hr, the thermocline was

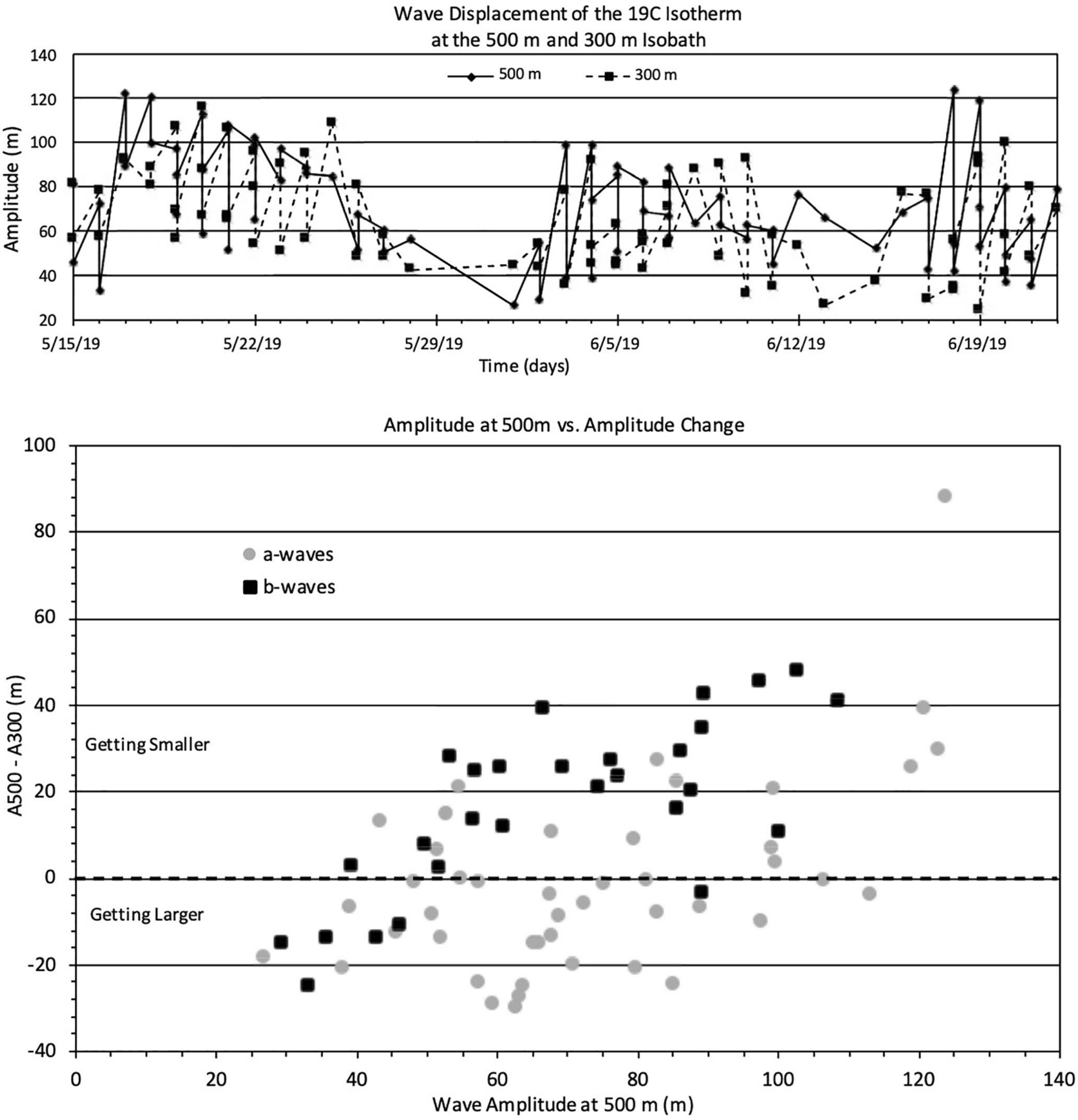

Figure 8. A comparison of the wave amplitude at the 500 and 300 m isobaths as a function of (a) time and (b) incident wave amplitude. The largest waves show reduced amplitude as they shoal, while the smaller waves continue to grow.

close to the surface and h_1 was less than h_2. At other times, for instance, centered around 0400 and 1800 hr at the 50, 20, and 10 m isobaths, the water column was homogeneous. The local tide was mixed, semidiurnal dominant, unlike the generating tide in the Luzon Straits which was mixed, diurnal dominant. The situation was complicated because the phase of each arriving trans-basin wave with respect to the phase of the local internal tide was constantly changing and this phasing is what determines the fate of each incoming wave.

What constitutes a “large” or a “small” NLIW? This is examined by plotting the change in wave amplitude between the 500 and 300 m isobaths as a function of time and wave amplitude (Figure 8). There were a few outliers, but generally speaking, smaller amplitude waves at T500 became larger at T300 and the larger waves became smaller. The trend was more obvious for the b-waves (black squares), with almost all waves larger than 50 m amplitude 500 m becoming smaller as they propagated onshore past the 300 m isobath (Figure 8b). Larger incident waves lost more amplitude than smaller ones. The situation was less clear for the a-waves (gray circles). Incident waves smaller than about 45 m continued to grow as they propagated shoreward. For incident wave amplitudes between 45 and 85 m, waves became both larger and smaller although more grew larger. Waves larger than 85 m amplitude typically became smaller as they shoaled. Since wave amplitude tracks the fortnightly cycle, these changes track it also, with large waves near spring tide getting smaller and smaller waves near neap tide becoming larger as they propagated toward the reef (Figure 8a).

These changes differ in detail but are conceptually similar to results from a 7-month time series just 43 km to the north (Chang, Lien, et al., 2021). Using an across-shore ADCP transect with moorings at 600, 430, and 350 m, they used westward wave velocity rather than amplitude to classify the size of the incident NLIWs. Strong waves with $U_{\max} > 1.6$ m s^{-1} weakened as they propagated from 600 to 430 m, while small waves ($U_{\max} < 1.2$ m s^{-1}) continued to grow. Both outcomes were observed for intermediate-sized waves with 1.6 m s$^{-1} > U_{\max} > 1.2$ m s^{-1}, analogous to the Dongsha waves with amplitudes between 45 and 85 m. They attribute their results to the ratio of $U_{\max}$ to the propagation speed C, which determines the onset of convective instability and limits the wave amplitude. Their changes observed from 600 to 430 m are analogous to our observed changes from 500 to 300 m. The reasons for these changes are discussed in greater detail below.

4. Discussion

We seek first to understand the relative phase speeds of the a- and b-waves and the rules governing when elevation waves will appear. For this task, the simple two-layer, weakly nonlinear solutions of the KdV equation will suffice. Strictly speaking, solitary waves in the environment are neither weakly nonlinear nor two-layer, however, these solutions have proven valuable for understanding the essential features of ocean observations (Grimshaw et al., 2010; Helfrich & Melville, 2006; Liu et al., 1998; Orr & Mignerey, 2003). On the middle Atlantic continental shelf, they also provided a reasonable approximation to the fully stratified solutions (Shroyer et al., 2009). The phase speed of a solitary wave based on the two-layer KdV equation is given by

$$C = c_0 + \frac{\eta_0}{3}\alpha \tag{1}$$

where c_0 is the linear phase speed, η_0 the wave amplitude, and α is the coefficient of nonlinearity, estimated in turn by

$$c_0^2 = \frac{g h_1 h_2 (\rho_2 - \rho_1)}{h_2 + h_1} \tag{2}$$

and

$$\alpha = \frac{3c_0}{2}\frac{h_1 - h_2}{h_1 h_2} \tag{3}$$

where h_1 and h_2 are the upper- and lower-layer thickness respectively, ρ_1 and ρ_2 the upper- and lower-layer density, and g the gravitational acceleration. Based on (1) the larger amplitude solitary waves are expected to travel faster due to the nonlinear contribution, however considering also (2) and (3), the propagation speed will be impacted by the local stratification that the waves are propagating into. Since the mean density in the upper and lower layers changed little, the contribution due to the stratification was dominated by changes in the layer thicknesses as the thermocline was pumped up and down by the local internal tide (Figure 5). The b-waves more frequently entered a region where the thermocline was depressed closer to mid-depth by the tide, and thus by (2) propagated 0.15 m s^{-1} faster than the a-waves on average. The local internal tide can also influence the apparent NLIW propagation speed by creating a following or opposing current (Alford et al., 2010; Fu et al., 2012).

The parameter α in (3) takes on special significance because the sign of α in the ambient (sometimes called upstream) water determines the polarity of the NLIWs that will form (Hsu & Liu, 2000; Liu et al., 2004; McSweeney et al., 2020; Orr & Mignerey, 2003; Shroyer et al., 2009). The depth where α changes sign ($\alpha = 0$) is called the critical depth and marks the turning point where depression waves will transition into elevation

Table 2
Positions and Bottom Characteristics for the Temperature Moorings Deployed East of Dongsha Reef

Name	Depth (m)	Lat (deg N)	Lon (deg E)	Separation (m)	Bottom slope	Slope degrees	Maximum amplitude	c (m/s)	$\lvert u\rvert/c$	Regime
PIES	2,000	20 41.837	118 04.323							
				102,000	0.009	0.54	180	2.6	<1	adiabatic
500T	503	20 41.983	117 04.985							
				8,988	0.021	1.21	100	1.8	<1	dispersion
300T2	313	20 41.759	116 59.806							
				6,355	0.035	1.99	60	1.1	>1	breaking, disintegration
100T	92	20 41.700	116 56.141							
				761	0.054	3.08	20	NA		disintegration, mixing
50M	51	20 41.965	116 55.806							
				511	0.059	3.35		NA		
20M	21	20 41.966	116 55.511							
				161	0.068	3.91		NA		
10M	10	20 41.987	116 55.421							

Note. Also shown are the maximum amplitudes and wave transformation processes expected from the expression $a_m > (H_b - H_m)0.4$. The mean propagation speed between locations is given by c and $|u|$ is the magnitude of the wave orbital velocity. An undisturbed upper layer thickness (thermocline depth) H_m of 50 m was used throughout.

waves. In deep water the lower layer is always thicker than the upper, the vorticity is positive, and depression waves prevail. Inshore of the critical point, the upper layer is thicker than the lower, the vorticity is negative, and elevation waves appear. In previous South China Sea studies the critical depth was sometimes taken to be constant at around 100–120 m (Liu et al., 2004) and the primary variability of α was treated as spatial. The important message here is that critical depth near Dongsha was not constant but rather changed radically according to the phase of the local internal tide (Figure 5). Thus, elevation waves could only form when the phase of the incident trans-basin solitary waves was a good match for local $h_1 > h_2$, which explains why so few of them were observed.

Understanding the actual transition process for shoaling NLIWs requires a more inclusive theory, such as the extended KdV (Gardner) equation or fully nonlinear numerical solutions (Grimshaw et al., 2010; Helfrich & Melville, 1986; Helfrich, 1992; Lamb, 2002; Lamb & Warn-Varnas, 2015; Rivera-Rosario et al., 2020; Vlasenko & Hutter, 2002; Vlasenko et al., 2005; Vlasenko & Stashchuk, 2007). These studies have shown that the most important factors determining NLIW behavior under shoaling are wave amplitude, bottom depth, bottom slope, and thermocline depth which is taken as the demarcation between the upper and lower layers. All these parameters can be easily estimated from the Donsgha transect data for comparison with the theory. The wave amplitude was determined by the 19°C isotherm depth as discussed above. The bottom depth and slope are available from the ship's hydrographic data set. The thermocline depth was estimated from the high-resolution T-string data and 14 XBTs deployed in the vicinity of the moorings. Taking the 23°C isotherm depth to represent the center of the thermocline, both data sets indicate an undisturbed thermocline depth of around 50m with little geographical variation around the moorings.

Four shoaling regimes emerge from the analysis which depend on the bottom slope and whether or not the wave velocity u is greater or less than the wave propagation speed c (Table 2). The bottom slope is considered gentle when it is less than 0.03 = 1.7° (Grimshaw et al., 2004; Lamb & Warn-Varnas, 2015; Rivera-Rosario et al., 2020; Vlasenko et al., 2005). Waves break when

$$a_m > (H_b - H_m)\,0.4 \tag{4}$$

where a_m is the maximum possible wave amplitude, H_b is the bottom depth, and H_m is the upper layer thickness, here approximated by thermocline depth (Helfrich & Melville, 1986; Helfrich, 1992; Vlasenko & Hutter, 2002). Offshore of 500 m, the bottom slope was very weak (0.54°), and u was always much less than c. Adiabatic shoaling is likely in this region (Grimshaw et al., 2010; Small, 2001a; Vlasenko et al., 2005). The PIES2000 data and previous moored data sets show that two-wave packets were already present for the a-waves between 1,500 m and 2,500 m depth (Ramp et al., 2010, 2019). The wave arrival patterns observed at the 500 m isobath are therefore similar to those in the deep basin. Between 500 and 300 m, the slope was greater (1.21°) but still gentle. The wave velocity u was still less than c for all the waves. When environmental conditions change too rapidly to allow adiabatic adjustment, but the bottom slope is still gentle, active dispersion occurs and solitary waves form packets as they shoal (Vlasenko & Hutter, 2002; Vlasenko & Stashchuk, 2007). This was evidenced for instance by the waves in Figure 5a and many other waves during the time series.

Continuing shoreward, two regimes were observed between 300 and 100 m. The bottom slope was still gentle (1.99°) at 300 m but then became steep (3.08°) at around 250 m up to 100 m on the slopes of the reef. The wave propagation speed c, which was mostly a function of bottom depth, continued to decrease while the orbital velocity remained about the same, resulting in $u > c$ for all the large waves. This condition resulted in active wave breaking due to both convective and Kelvin-Helmholtz instability between 300 and 250 m (Chang, 2021; Chang, Cheng, et al., 2021). Trapped cores may also form under these circumstances (Chang, Cheng, et al., 2021) as has been previously observed near Dongsha (Lien et al., 2012, 2014). Prior to reaching the 100 m isobath, most large waves either disintegrated or were transformed into elevation waves, which continued to propagate farther onshore.

The limiting wave amplitudes were also consistent with (Equation 4; Table 2). Waves larger than 150 m have only rarely been observed at 500 m consistent with the suggestion that waves up to 180 m may be possible (Table 2, column 8). The results suggest that depression waves with amplitude larger than 60 m will be transformed by the 100 m isobath, which shows reasonable agreement with the data although some slightly larger waves occasionally remained observable. This was likely due to temporal (tidal) variation of H_m (Figure 5d) which was considered constant for Table 2, and other environmental variability not accounted for by a simple two-layer theory such as the local wind stress and background shear. Smaller upper layer thickness admits the possibility of larger depression waves surviving farther upslope. It is noteworthy that a more generalized criteria for determining NLIW breaking versus dispersion which includes the bottom slope (Vlasenko & Hutter, 2002) did not improve results here, admitting waves that were much too large at each isobath. Their expression apparently only applies to steeper bottom slopes than those observed here.

Three properties of the type a-versus type b-waves are especially salient to understanding the wave shoaling problem (Figure 2). First, incident a-waves almost all arrived at T500 as two or three-wave packets while the b-waves were solitary. This is because the a-waves are more energetic than the b-waves exiting the generation region since the b-waves experience higher dissipation over the northern Heng-Chun Ridge (Alford et al., 2011). Second, the largest a-waves arrived earlier in the fortnightly cycle, before or near spring tide, while the largest b-waves arrived later in the fortnightly cycle. The largest b-waves were just as large as the largest a-waves. The reason for this is not clear but presumably depends on the details of the barotropic tidal forcing in the Luzon Strait. Third, and perhaps most importantly, the mean angle of incidence for the b-waves was almost due west (258°) while the a-waves were headed about 29° farther north (287°). This is a product of the b-waves being generated in the northern reaches of the Luzon Strait and the a-waves farther south (Du et al., 2008; Ramp et al., 2019; Zhang et al., 2011). The consequence of this is that the b-waves strike the Dongsha Reef almost dead on, while the a-waves strike a more glancing blow, effectively reducing the bottom slope presented to the incoming wave. This partially explains why a-waves of a given amplitude survive farther up the slope than similar b-waves. Additionally, the reef is not perfectly round, and the mooring transect occupies a promontory that extends eastward and has slopes that are steeper than to the north and south. The a-waves approaching from the southwest travels farther westward over the gentler slope before encountering the steeper slopes over the promontory. These differences between the waves may also be important in understanding the reflection and refraction phenomena, which will be considered in a future analysis.

5. Conclusions

An array of oceanographic moorings and a DTS cable were deployed over the eastern slope of Dongsha Reef in the northeastern South China Sea from the 2,000 m isobath to the reef crest, during May and June 2019. The dominant oceanographic signal observed was caused by very large nonlinear internal waves of depression impinging on the reef and propagating upslope into shallower water. The waves are important because their vertical motions nourish the reef ecology, and their strong currents and buoyancy fluctuations disrupt marine operations around the reef. This is the first time the wave progression has been documented from the deep basin to the surf zone near Dongsha. By sampling for three complete fortnights, a wide range of incident nonlinear wave amplitudes from 30 to 122 m were studied.

The NLIW arrival patterns observed at the 2,000 m PIES instrument and 500 m mooring were due to the trans-basin waves which were generated by the interaction of the barotropic tide with bottom topography in the Luzon Strait and propagated WNW across the sea. The amplitude of the arriving waves closely tracked the fortnightly envelope for the tidal forcing, delayed by the propagation time of 51.6 hr. The type a- and b-waves identified by many previous authors were readily apparent. The a-waves were generally but not always larger than the b-waves and consisted of 2–3 wave packets on arrival at the transect. The b-waves were larger toward the end of the fortnightly cycle and were usually solitary in the deep basin, forming packets only upon shoaling up the upper continental slope. Importantly for the shoaling process, the b-waves propagated almost due west and struck the reef complex straight on, while the a-waves propagated 29° more northward and struck a more glancing blow. As a result, the b-waves interacted more strongly with the bottom than the a-waves, forming more packets and breaking sooner.

Four regions of wave transformation were identified in the cross-slope direction. Offshore of 500 m, the wave shoaling was adiabatic with little change of form. Between 500 and 300 m, wave dispersion dominated via packet formation. This reduced the amplitude of the leading wave for the largest waves. From 300 to 250 m, wave breaking via both convection and Kelvin-Helmholtz instability was the dominant process (Chang, Cheng, et al., 2021). Shoreward of 250 m, the bottom became quite steep and most of the large waves disintegrated via breaking and strong mixing. Some waves successfully transitioned to elevation waves when they encountered a thermocline near the bottom (upper layer thickness greater than lower) and continued propagating shoreward past the 100 m isobath. These waves forced cold water upslope along the bottom to less than 15 m depth in the DTS cable data, and potentially play an important role in nourishing the reef.

Data Availability Statement

All data used in this paper including temperature, salinity, velocity, inverted echo sounder travel times, and DTS cable temperature data are available in the Meldeley Data Repository and may be accessed via https://data.mendeley.com/datasets/hgwtm2g36n/2. This is an open link available to all.

Acknowledgments
This work was supported by the U. S. Office of Naval Research under grants N00014-19-1-2686 (322 MM) for the field work, N00014-20-1-2727 (322PO) for the data analysis to S. R. Ramp, and N00014-19-WX-00466 (321OA) to D. B. Reeder. K. A. Davis and G. Sinnett were supported by NSF Grant No. OCE-1753317. Ship time and Taiwanese participation was funded by the Taiwanese Ministry of Science and Technology (MOST). Mr. Wen-Hwa Her (IONTU) designed, deployed and recovered the moorings. We thank the officers and crew of the R/V OCEAN RESEARCHER III for their patience and skill executing the work at sea.

References

Aghsaee, P., & Boegman, L. (2015). Experimental investigation of sediment resuspension beneath internal solitary waves of depression. *Journal of Geophysical Reseaarch Oceans*, *120*, 3301–3314. https://doi.org/10.1002/2014JC010401

Alford, M. H., Lien, R.-C., Simmons, H., Klymak, J., Ramp, S. R., Yang, Y.-J., et al. (2010). Speed and evolution of nonlinear internal waves transiting the South China Sea. *Journal of Physical Oceanography*, *40*, 1338–1355. https://doi.org/10.1175/2010jpo4388.1

Alford, M. H., MacKinnon, J. A., Nash, J. D., Simmons, H., Pickering, A., Klymak, J. M., et al. (2011). Energy flux and dissipation in Luzon Strait: Two tales of two ridges. *Journal of Physical Oceanography*, *41*, 2211–2222. https://doi.org/10.1175/jpo-d-11-073.1

Alford, M. H., Peacock, T., co-authors, J. A., Nash, J. D., Buijsman, M. C., Centurioni, L. R., et al. (2015). The formation and fate of internal waves in the South China Sea. *Nature*, *521*, 65–69. https://doi.org/10.1038/nature14399

Bai, X., Li, X., Lamb, K., Hu, J., & Hu, J. (2017). Internal solitary wave reflection near Dongsha atoll, the south China sea. *Journal of Geophysical Research Oceans*, *122*, 7978–7991. https://doi.org/10.1002/2017JC012880

Bogucki, D. J., Redekopp, L. G., & Barth, J. (2005). Internal solitary waves in the coastal mixing and optics 1996 experiment: Multimodal structure and resuspension. *Journal of Geophysical Research Oceans*, *110*, C02024. https://doi.org/10.1029/2003JC002253

Chang, M.-H. (2021). Marginal instability within internal solitary waves. *Geophysical Research Letters*, *48*. https://doi.org/10.1029/2021GL092616

Chang, M.-H., Cheng, Y.-H., Yang, Y.-J., Jan, S., Ramp, S. R., Reeder, D. B., et al. (2021). Direct measurements reveal instabilities and turbulence within large amplitude internal solitary waves beneath the ocean. *Communications Earth & Environments*, *2*(15), 1–10. https://doi.org/10.1038/S43247-020-00083-6

Chang, M.-H., Lien, R.-C., Lamb, K. G., & Diamessis, P. J. (2021). Long-term observations of shoaling internal solitary waves in the northern South China Sea. *Journal of Geophysical Research Oceans*, *126*, e2020JC017129. https://doi.org/10.1029/2020JC017129

Chen, Y.-J., Ko, D. S., & Shaw, P.-T. (2013). The generation and propagation of internal solitary waves in the South China Sea. *Journal of Geophysics Research Oceans*, *118*, 6578–6589. https://doi.org/10.1002/2013JC009319

Chiu, C.-S., Ramp, S. R., Miller, C. W., Lynch, J. F., Duda, T. F., & Tang, T.-Y. (2004). Acoustic intensity fluctuations induced by South China Sea internal tides and solitons. *IEEE/Journal of Oceanic Engineering*, *29*, 1249–1263. https://doi.org/10.1109/joe.2004.834173

Chiu, L. Y. S., Reeder, D. B., Chang, Y.-Y., Chen, C.-F., Chiu, C.-S., & Lynch, J. (2013). Enhanced acoustic mode coupling resulting from an internal solitary wave approaching the shelfbreak in the South China Sea. *Journal of the Acoustical Society of America*, *133*, 1306–1319. https://doi.org/10.1121/1.4789358

Davis, K. A., Arthur, R. S., Reid, E. C., Rogers, J. S., Fringer, O. B., DeCarlo, T. M., & Cohen, A. L. (2020). Fate of internal waves on a shallow shelf. *Journal of Geophysical Research: Oceans*, *125*, e2019JC015377. https://doi.org/10.1029/2019jc015377

Diamessis, P. J., & Redekopp, L. G. (2006). Numerical investigation of solitary internal wave-induced global instability in shallow water benthic boundary layers. *Journal of Physical Oceanography*, *36*, 784–812. https://doi.org/10.1175/jpo2900.1

Du, T., Tseng, Y.-H., & Yan, X.-H. (2008). Impacts of tidal currents and Kuroshio intrusion on the generation of nonlinear internal waves in Luzon Strait. *Journal of Geophysical Research Oceans*, *113*, C080015. https://doi.org/10.1029/2007JC004294

Duda, T. F., Lynch, J. F., Newhall, A. E., Wu, L., & Chiu, C.-S. (2004). Fluctuation of the 400 Hz sound intensity in the 2001 ASIAEX South China Sea experiment. *IEEE/Journal of Oceanic Engineering*, *29*, 1264–1279. https://doi.org/10.1109/joe.2004.836997

Egbert, G., & Erofeeva, S. (2002). Efficient inverse modeling of barotropic ocean tides. *Journal of Atmospheric and Oceanic Technology*, *19*, 183–204. https://doi.org/10.1175/1520-0426(2002)019<0183:eimobo>2.0.co;2

Farmer, D. M., Alford, M. H., Lien, R.-C., Yang, Y. J., Chang, M.-H., & Li, Q. (2011). From Luzon Strait to Dongsha Plateau: Stages in the life of an internal wave. *Oceanography*, *24*, 64–77. https://doi.org/10.5670/oceanog.2011.95

Fu, K.-H., Wang, Y.-H., Laurent, L. S., Simmons, H., & Wang, D.-P. (2012). Shoaling of large-amplitude nonlinear internal waves at Dongsha Atoll in the northern South China Sea. *Continental Shelf Research*, *37*, 1–7. https://doi.org/10.1016/j.csr.2012.01.010

Grimshaw, R., Pelinovsky, E. N., Talipova, T. G., & Kurkina, A. (2004). Simulations of the transformation of internal solitary wave on oceanic shelves. *Journal of Physical Oceanography*, *34*, 2774–2791. https://doi.org/10.1175/jpo2652.1

Grimshaw, R., Pelinovsky, E. N., Talipova, T. G., & Kurkina, A. (2010). Internal solitary waves: Propagation, deformation and disintegration. *Nonlinear Processes in Geophysics*, *17*, 633–649. https://doi.org/10.5194/npg-17-633-2010

Helfrich, K. R. (1992). Internal solitary wave breaking and run-up on a uniform slope. *Journal of Fluid Mechanics*, *243*, 133–154. https://doi.org/10.1017/s0022112092002660

Helfrich, K., & Grimshaw, R. (2008). Nonlinear disintegration of the internal tide. *Journal of Physical Oceanography*, *38*(3), 686–701. https://doi.org/10.1175/2007JPO3826.1

Helfrich, K. R., & Melville, W. K. (1986). On long nonlinear internal waves over slowly varying topography. *Journal of Fluid Mechanics*, *149*, 305–317.

Helfrich, K. R., & Melville, W. K. (2006). Long nonlinear internal waves. *Annual Reviews of Fluid Mechanics*, *38*, 395–425. https://doi.org/10.1146/annurev.fluid.38.050304.092129

Hsu, M.-K., & Liu, A. K. (2000). Nonlinear internal waves in the south China sea. *Canadian Journal of Remote Sensing*, *26*, 72–81. https://doi.org/10.1080/07038992.2000.10874757

Jackson, C. B. (2009). An empirical model for estimating the geographic location of nonlinear internal solitary waves. *Journal of Atmospheric and Oceanic Technology*, *26*, 2243–2255. https://doi.org/10.1175/2009jtecho638.1

Jia, T., Liang, J. J., Li, X.-M., & Sha, J. (2018). Observation and numerical simulation of internal solitary wave refraction and reconnection behind the Dongsha Atoll. *Journal of Geophysical Research: Oceans*, *123*, 74–89. https://doi.org/10.1002/2017JC013389

Lamb, K. G. (2002). A numerical investigation of solitary internal waves with trapped cores formed via shoaling. *Journal of Fluid Mechanics*, *451*, 109–144. https://doi.org/10.1017/s002211200100636x

Lamb, K. G., & Warn-Varnas, A. (2015). Two-dimensional numerical simulations of shoaling internal solitary waves at the ASIAEX site in the South China Sea. *Nonlinear Processes in Geophysics*, *22*, 289–312. https://doi.org/10.5194/npg-22-289-2015

Li, Q., & Farmer, D. M. (2011). The generation and evolution of nonlinear internal waves in the deep basin of the South China Sea. *Journal of Physical Oceanography*, *41*, 1345–1363. https://doi.org/10.1175/2011jpo4587.1

Li, Q., Farmer, D. M., Duda, T. F., & Ramp, S. R. (2009). Acoustical measurement of nonlinear internal waves using the inverted echo sounder. *Journal of Atmospheric and Oceanic Technology*, *26*, 2228–2242. https://doi.org/10.1175/2009jtecho652.1

Li, X., Jackson, C. R., & Pichel, W. G. (2013). Internal solitary wave refraction at Dongsha atoll, south China sea. *Geophysical Research Letters*, *40*, 3128–3132. https://doi.org/10.1002/grl.50614

Li, Q., Wang, B., Chen, X., Chen, X., & Park, J.-H. (2016). Variability of nonlinear internal waves in the South China Sea affected by the Kuroshio and mesoscale eddies. *Journal of Geophysical Research-Oceans*, *121*, 2098–2118. https://doi.org/10.1002/2015JC011134

Lien, R. C., D'Asaro, E. A., Henyey, F., Chang, M.-H., Tang, T. Y., & Yang, Y. J. (2012). Trapped core formation within a shoaling nonlinear internal wave. *Journal of Physical Oceanography*, *42*, 511–525. https://doi.org/10.1175/2011jpo4578.1

Lien, R. C., Henyey, F., Ma, B., & Yang, Y. J. (2014). Large-amplitude internal solitary waves observed in the northern South China Sea: Properties and Energetics. *Journal of Physical Oceanography*, *44*, 1095–1115. https://doi.org/10.1175/jpo-d-13-088.1

Liu, A. K., Chang, Y. S., Hsu, M.-K., & Liang, N. K. (1998). Evolution of nonlinear internal waves in the east and south China seas. *Journal of Geophysical Research*, *103*, 7995–8008. https://doi.org/10.1029/97jc01918

Liu, A. K., Ramp, S. R., Zhao, Y., & Tang, T. Y. (2004). A case study of internal solitary wave propagation during ASIAEX 2001. *IEEE/Journal of Ocean Engineering*, *29*, 1144–1156. https://doi.org/10.1109/joe.2004.841392

McSweeney, J. M., Lerczak, J. A., Barth, J. A., Becherer, J., Colosi, J. A., MacKinnon, J. A., et al. (2020). Observations of shoaling nonlinear internal bores across the central California inner shelf. *Journal of Physical Oceanography*, *50*, 111–132. https://doi.org/10.1175/jpo-d-19-0125.1

Orr, M. H., & Mignerey, P. C. (2003). Nonlinear internal waves in the South China Sea: Observations of the conversion of depression internal waves to elevation internal waves. *Journal of Geophysical Research*, *108*, 3064. https://doi.org/10.1029/2001JC001163

Park, J.-H., & Farmer, D. (2013). Effects of Kuroshio intrusions on nonlinear internal waves in the South China Sea during winter. *Journal of Geophysical Research-Oceans*, *118*, 7081–7094. https://doi.org/10.1002/2013JC008983

Ramp, S. R., Chiu, C.-S., Bahr, F. L., Qi, Y., Dahl, P. H., Miller, J. H., et al. (2004). The shelf-edge environment in the central east China Sea and its impact on low frequency acoustic propagation. *IEEE/Journal of Ocean Engineering*, *29*, 1011–1031. https://doi.org/10.1109/joe.2004.840842

Ramp, S. R., Chiu, C.-S., Kim, H.-R., Bahr, F. L., Tang, T. Y., Yang, Y.-J., et al. (2004). Solitons in the northeastern South China sea Part I: Sources and propagation through deep water. *IEEE/Journal of Ocean Engineering*, *29*, 1157–1181. https://doi.org/10.1109/joe.2004.840839

Ramp, S. R., Park, J.-H., Yang, Y.-J., Bahr, F. L., & Jeon, C. (2019). Latitudinal structure of solitons in the south China sea. *Journal of Physical Oceanography*, *49*, 1747–1767. https://doi.org/10.1175/jpo-d-18-0071.1

Ramp, S. R., Yang, Y.-J., & Bahr, F. L. (2010). Characterizing the nonlinear internal wave climate in the northeastern South China Sea. *Nonlinear Processes in Geophysics*, *17*, 481–498. https://doi.org/10.5194/npg-17-481-2010

Reeder, D. B., Chiu, L., & Chen, C.-F. (2010). Experimental evidence of horizontal refraction by non-linear internal waves of elevation in shallow water in the south China sea: 3D vs. Nx2D acoustic propagation modeling. *Journal of Theoretical and Computational Acoustics*, *18*, 267–278. https://doi.org/10.1142/s0218396x10004176

Reeder, D. B., Ma, B., & Yang, Y.-J. (2010). Very large subaqueous sand dunes on the upper continental slope in the South China Sea generated by episodic, shoaling deep-water internal solitary waves. *Marine Geology*, *279*, 12–18.

Reid, E. C., DeCarlo, T. M., Cohen, A. L., Wong, G. T. F., Lentz, S. J., Safaie, A., et al. (2019). Internal waves influence the thermal and nutrient environment on a shallow coral reef. *Limnology & Oceanography*, *64*(5), 1–17. https://doi.org/10.1002/lno.11162

Rivera-Rosario, G., Diamesis, P. J., Lien, R.-C., Lamb, K. G., & Thomsen, G. N. (2020). Formation of recirculating cores in convectively breaking internal solitary waves of depression shoaling over gentle slopes in the south China Sea. *Journal of Physical Oceanography*, *50*, 1137–1157. https://doi.org/10.1175/jpo-d-19-0036.1

Rogers, J. S., Rayson, M. D., Ko, D. S., Winters, K. B., & Fringer, O. (2019). A framework for seamless one-way nesting of internal wave-resolving ocean models. *Ocean Modeling*, *143*, 101462. https://doi.org/10.1016/j.ocemod.2019.101462

Shroyer, E. L., Moum, J. N., & Nash, J. D. (2009). Observations of polarity reversal in shoaling nonlinear internal waves. *Journal of Physical Oceanography*, *39*, 691–701. https://doi.org/10.1175/2008jpo3953.1

Sinnett, G., Davis, K. A., Lucas, A., Giddings, S. N., Reid, E., Harvey, M. E., & Stokes, I. (2020). Distributed temperature sensing for oceanographic applications. *Journal of Atmospheric Ocean Techniques*, *37*(11), 1987–1997. https://doi.org/10.1175/jtech-d-20-0066.1

Sinnett, G., Ramp, S. R., Yang, Y. J., Chang, M.-H., Jan, S., & Davis, K. A. (2021). Large amplitude internal wave transformations into shallow water. Manuscript submitted for publication.

Small, J. (2001a). A nonlinear model of the shoaling and refraction of interfacial solitary waves in the ocean. Part I: Development of the model and investigations of the shoaling effect. *Journal of Physical Oceanography*, *31*, 3163–3183. https://doi.org/10.1175/1520-0485(2001)031<3163:anmots>2.0.co;2

Small, J. (2001b). A nonlinear model of the shoaling and refraction of interfacial solitary waves in the ocean. Part II: Oblique refraction across a continental slope and propagation over a seamount. *Journal of Physical Oceanography*, *31*, 3184–3199. https://doi.org/10.1175/1520-0485(2001)031<3184:anmots>2.0.co;2

Stastna, M., & Lamb, K. G. (2008). Sediment resuspension mechanisms associated with internal waves in coastal waters. *Journal of Geophysical Research Oceans*, *113*, C10016. https://doi.org/10.1029/2007JC004711

Vlasenko, V., Guo, C., & Stashchuk, N. (2012). On the mechanism of A-type and B-type internal solitary wave generation in the northern South China Sea. *Deep-Sea Research I*, *69*, 100–112. https://doi.org/10.1016/j.dsr.2012.07.004

Vlasenko, V., & Hutter, K. (2002). Numerical experiments on the breaking of solitary internal waves over a slope-shelf topography. *Journal of Physical Oceanography*, *32*, 1779–1793. https://doi.org/10.1175/1520-0485(2002)032<1779:neotbo>2.0.co;2

Vlasenko, V., Ostrovsky, L., & Hutter, K. (2005). Adiabatic behavior of strongly nonlinear internal solitary waves in slope-shelf areas. *Journal of Geophysical Research*, *110*, C04006. https://doi.org/10.1029/2004JC002705

Vlasenko, V., & Stashchuk, N. (2007). Three-dimensional shoaling of large-amplitude internal waves. *Journal of Geophysical Research-Oceans*, *112*, C11018. https://doi.org/10.1029/2007JC004107

Wang, Y.-H., Dai, C.-F., & Chen, Y.-Y. (2007). Physical and ecological processes of internal waves on an isolated reef ecosystem in the South China Sea. *Geophysical Research Letters*, *34*, 1–7. https://doi.org/10.1029/2007GL030658

Yang, Y.-J., Tang, T. Y., Chang, M. H., Liu, A. K., Hsu, M.-K., & Ramp, S. R. (2004). Solitons northeast of Tung-Sha Island during the ASIEAX pilot studies. *IEEE/Journal of Ocean Engineering*, *29*, 1182–1199. https://doi.org/10.1109/joe.2004.841424

Zhang, Z., Fringer, O. B., & Ramp, S. R. (2011). Three-dimensional, nonhydrostatic numerical simulation of nonlinear internal wave generation and propagation in the South China Sea. *Journal of Geophysical Research-Oceans*, *116*, C05022. https://doi.org/10.1029/2010JC006424

Zhao, Y., Liu, A. K., & Hsu, M. K. (2008). Internal wave refraction observed from sequential satellite images. *International Journal of Remote Sensing*, *29*(21), 6381–6390. https://doi.org/10.1080/01431160802175520